International Journal for Housing Science and Its Applications
Publish August 4, 2025. Volume 46, Issue 3 Pages 3035-3045

https://doi.org/10.70517/ijhsa463254

Numerical simulation of nonlinear optical effects in solid state physics based on finite element analysis

Zhiwei He[1,*]
[1] Puyang Institute of Technology, Henan University, West Section of Yellow RiverRoad, Puyang, Henan, 457000, China
Corresponding authors: (e-mail: 1350013005@sqgxy.edu.cn).

Abstract The second-order nonlinear optical effects that may arise from the interaction between solid materials and light are the current research hotspots in the field of laser technology. In this paper, the nonlinear optical effects and characteristics in solid state physics are taken as the research object, and the finite element analysis technique, which has higher solution accuracy and can get rid of the limitations of actual physical conditions, is adopted as the research tool. The steps of FEA model generation are explained. Then, three common second-order optical frequency conversion phenomena in one-dimensional nonlinear photonic crystals are summarized, and the corresponding phase matching methods are presented. On this basis, the intrinsic physical mechanisms and processes of various nonlinear optical effects in the optoelectronic integration platform (SOI optical waveguide) are discussed. The theoretical modeling framework of various nonlinear optical effects in different solid-state physical materials is thus formed. With the technical support of the above analytical methods and theoretical models, a mode-locked fiber laser is designed for pulsed laser applications based on the nonlinear optical characteristics of the solid-state physical material graphyne. The laser was tested experimentally for 10h and the output power was kept at 2.31mW with good stability.

Index Terms nonlinear optical effects, finite element analysis, second-order optical frequency conversion, solid-state physical materials

I. Introduction

Laser technology is one of the most important inventions after atomic energy, computers and semiconductors, and is widely used in the fields of LIDAR and weapons, laser scanning and ranging, and fiber optic communications [1], [2]. However, the available lasers of different wavelengths are limited and the wavelength range of lasers must be broadened by laser frequency conversion media to achieve the wavelength requirement of light [3], [4]. Solid physical materials with nonlinear optical effects are indispensable advanced laser materials by utilizing the frequency doubling effect to achieve laser frequency conversion [5]. China has carried out a lot of exploration in the field of nonlinear optical materials, however, the types and numbers of existing materials are still very limited, and the new band of high-performance nonlinear optical materials are facing a serious situation of practical difficulties [6]-[8]. In addition, the synthesis methods of nonlinear optical materials still continue the traditional trial-and-error method, which is difficult to meet the increasing demand for materials [9], [10]. Therefore, there is an urgent need for the intervention of high-throughput computational research methods for materials to effectively reduce the experimental cost, shorten the R&D cycle, efficiently develop the new generation of deep UV/IR nonlinear optical materials, and consolidate China's traditional dominant position in this research field and related science and technology industries.

Currently, some important research results have been achieved in the analysis and prediction of nonlinear optical materials. For example, literature [11] introduces a variety of theoretical calculations oriented to the design of high-order nonlinear optical materials, which promotes the experimental synthesis of organic and inorganic nonlinear optical materials and contributes to the rapid development of the field of optoelectronics. Literature [12] shows that the topological quantities of Berry connection and Berry curvature can be used to characterize the nonlinear optical effects of solid materials under specific conditions, and thus mastering the relationship between the topological view of the vector field in the momentum and parameter space can effectively facilitate the design of nonlinear optical materials. Literature [13] evaluated the optical transmission properties of a photonic crystal fiber with a D-type structure using the finite element method, and the resulting numerical simulation results provide data support for nonlinear applications. Literature [14] analyzed the nonlinear optical properties of the material to fit the corresponding optical limiting effect function as a nonlinear activation function, thus constructing an all-optical diffractive deep neural network modeling method, and the simulation results provide theoretical references for

related engineering based on nonlinear optical materials. Literature [15] applies the ultrashort pulse mathematical model to the analysis process of optical fiber properties, through the construction of the dynamic function that can describe the atomic dynamics and physical behavior of the quantum mechanical system, so as to accurately test the nonlinear optical wave-like properties possessed by optical fiber materials.

In this paper, we first establish the geometrical structure and demonstrate the steps and processes of generating finite element models for solid object materials. Then, it describes in detail the nonlinear Bragg diffraction, nonlinear Ramanas diffraction, and nonlinear Cherenkov radiation in low-dimensional nonlinear photonic crystals, totaling three kinds of second-order optical frequency conversion and phase matching operations. Meanwhile, based on the optoelectronic integration platform (SOI optical waveguide), the nonlinear optical processes of dispersion, linear loss, self-phase modulation, Raman scattering, two-photon absorption and other effects are discussed, and the basic forms of theoretical models corresponding to a variety of nonlinear optical effects are proposed. Finally, the analysis of the nonlinear optical generation process of the four-wave mixing effect in graphene materials, the evaluation of the application of graphene materials in the field of pulsed lasers, and the analysis of the ferroelectric properties of monolayers of group V elements are developed, respectively.

II. Finite element model generation

Models in finite element software can be categorized into solid models, trusses, beams, shell units and hybrid unit models. Solid model represents the solid structure with three-dimensional solid units, which is the most widely used form at present. The shell unit model simplifies the solid into a thin-layer structure, which can reduce the amount of calculation and storage, and is suitable for analyzing the static mechanical properties of solids. The truss and beam models consider the solid as a space frame structure composed of linear elastic rods or beams respectively, which can simulate the fiber structure of the solid. The hybrid unit model, on the other hand, treats the solid as a hybrid structure composed of different units, which can characterize a variety of mechanical properties of the solid, but needs to deal with the connection and coupling problems between different units.

After the solid geometry is established, the solid geometry needs to be discretized into a limited number of cells through grid generation, and commonly used grids include adaptive grids and regular grids. The former is usually used in solid mechanics modeling, and the appropriate number of nodes and cells need to be selected when generating the adaptive mesh in order to achieve a balance between computational accuracy and efficiency. Knitting coils are divided into four categories under different grid densities: 3023 elements, 15165 elements, 32137 elements, and 110180 elements, and the denser the mesh is divided into, the more accurate the results of the computation are but the longer the computation time is also. . In addition to the grid, the units selected for model generation are also different, and the commonly used units include hexahedron and tetrahedron, etc., and each small unit can be described by nodes. After completing the above settings, a solid finite element model can be obtained by selecting a suitable material intrinsic model coupled with a finite element mesh according to the research needs.

III. Theoretical framework for nonlinear optical effects

III. A. Second-order nonlinear optical phenomena in nonlinear photonic crystals

The arbitrary polarization configurations of ferroelectric domains in the space of nonlinear photonic crystals theoretically provide rich phase-matching possibilities for nonlinear frequency conversion processes within the crystals, giving nonlinear photonic crystals the potential to construct novel nonlinear structures. In the conventional quasi-phase-matching process, the fundamental-frequency wave and the crystal inverted lattice vector direction are co-linear, resulting in co-linear harmonics. When the direction of the incident fundamental frequency light and the crystal inverted lattice vector are no longer co-linear, the harmonics will be diffracted at non-co-linear positions to satisfy the corresponding matching conditions, and the distribution of some of the harmonic diffraction fields is very similar to that of the linear light field traveling through a grating. For example, when the incident light field is incident at a certain angle to the second-order nonlinear coefficients of the periodic modulation of the nonlinear grating, the second harmonic of the Bragg diffraction type will be generated. And when the phase matching condition is satisfied for the Bragg-type diffracted second harmonic in only some of the directions, Ramanas-type and Cherenkov-type second harmonics can be generated based on the difference in directions. This actually corresponds to the second-order nonlinear Bragg diffraction (NBD), nonlinear Ramanas street emission (NRND) and nonlinear Cherenkov radiation (NCR) phenomena.

III. A. 1) Nonlinear Bragg diffraction

In nonlinear period-modulated crystals, when the fundamental frequency light incidence direction and the crystal period-modulation direction are perpendicular to each other, nonlinear Bragg diffraction occurs if the strict Bragg

conditions are satisfied. The automatic transverse matching of vector triangles produces nonlinear Ramanas diffraction See Fig. 1, when Bragg diffraction occurs, the fundamental wavevector, crystal inverted lattice vector, and second harmonic wavevector form a complete vector triangle, which satisfies Eq. (1) between them:

$$2\vec{k}_1 + m\vec{G}_0 = \vec{k}_2 \tag{1}$$

where, $G_0 = \frac{2\pi}{\Lambda}$ is the unit inverse lattice vector of the crystal, Λ is the modulation period of the crystal polarization, m is the number of levels of the crystal's inverse lattice vector.

The Bragg diffraction angle is $\theta = \arccos\frac{2k_1}{k_2}$.

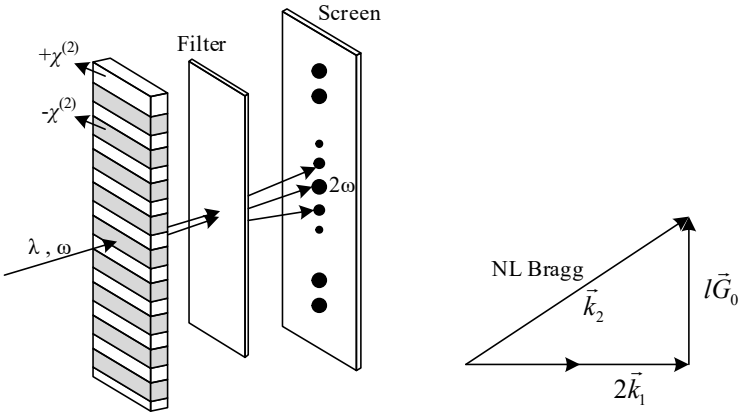

(a) Nonlinear Bragg diffraction occurs when the incident direction of the fundamental frequency light is perpendicular to the periodic modulation direction of the crystal.

(b) The phase-matching vector triangle of nonlinear Bragg diffraction.

Figure 1: Diagram of nonlinear Bragg diffraction

As can be seen from the required phase-matching vector triangles in Fig. 1(b), the conditions for the generation of nonlinear Bragg diffraction are very stringent, with exact requirements for the wavelength of the incident optical field and the modulation period of the crystal nonlinear coefficients. However, for bulk media, the existing polarization technology has not yet been able to realize the polarization modulation with very small period, which makes the inverted lattice vectors of the period-polarized crystals used in practice relatively small, and it is generally very difficult to satisfy such a complete vector triangle phase matching condition. In general, the refractive index of the crystal can be changed by adjusting the temperature to realize the complete phase matching. Alternatively, the shape of the vector triangle can be adjusted in the inverse space by changing the angle of incidence of the fundamental frequency light, which reduces the requirement of the complete vector triangle on the size of the crystal inverted lattice vector. The phase matching of a fundamental wave obliquely incident on a one-dimensional photonic crystal to produce nonlinear Bragg diffraction is shown in Fig. 2, and the matching of the full vector triangle can be realized by obliquely incident fundamental frequency light when the modulation period of the crystal is determined. In addition, the outgoing nonlinear Bragg diffraction of different orders can be realized by adjusting the angle of incidence.

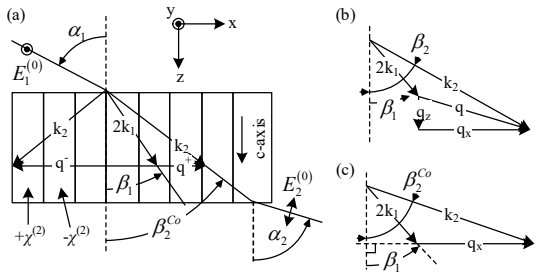

Figure 2: Phase matching generated by oblique incident photonic crystals

III. A. 2) Nonlinear Ramanas diffraction

If the directional relationship between the incident light field and the crystal's nonlinear periodic modulation phase can be perpendicular is not altered, there is a natural mismatch in the longitudinal direction of the vector triangle due to the small crystal inversion vectors in practice. However, this mismatch in the partial direction of the vector triangle still produces a certain efficiency of frequency conversion, which generates the more common nonlinear Ramanas diffraction. Figure 3 shows the automatic transverse matching of vector triangles generating nonlinear Ramanas diffraction, with a phase mismatch in the longitudinal direction of propagation that is satisfied by a phase match in the transverse direction. This type of phase matching in a portion of space that is naturally satisfied depending on the size of the crystal's inverted lattice vector is known as the automatic transverse phase matching process. It also implies that experimentally multiple levels of nonlinear Ramanas diffraction can be observed, with the diffraction angles of the different levels satisfying Eq. (2):

$$\theta_m = \arcsin\frac{mG_0}{k_2} \tag{2}$$

Due to the partial phase matching in space, the conversion efficiency and intensity are weaker than that of nonlinear Bragg diffraction. The conversion efficiency and strength are weaker than that of nonlinear Bragg diffraction due to partial phase matching in space.

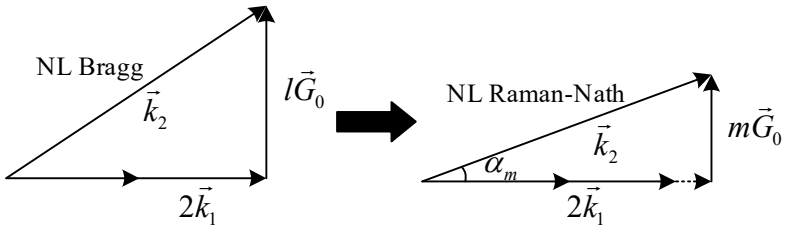

Figure 3: Diagram of nonlinear Raman-Nath diffraction

III. A. 3) Nonlinear Cherenkov radiation

In experiments in which nonlinear Ramanas diffraction is observed, two second-harmonic light spots whose positions are not modulated by the lattice inversion lattice vector are observed symmetrically distributed along the fundamental frequency of light, and whose production is independent of the lattice modulation period and is related only to the dispersion relation of the crystal, as nonlinear Cherenkov radiation.

Cherenkov-type radiation phenomena were first produced in particle physics experiments when charged particles were found to exceed the speed of light in a medium. The bound charge in the medium produces induced current due to the excitation of the moving charged particles, and when the moving particles exceed the speed of light in the medium, the sub-wave source generated by its induced current produces a conical wave front, and the conical wave fronts generated at different locations are coherently superimposed at a specific angle to produce Cherenkov radiation, which is called the Cherenkov angle, and satisfies equation (3):

$$\cos\theta = \frac{c/n}{v} \tag{3}$$

where, c is the vacuum speed of light, n is the refractive index of the medium, and v is the speed of particle motion. It can be seen that Cherenkov radiation is produced only when the speed of moving electrons exceeds the speed of light in the medium. And when the speed of moving electrons is less than the speed of light in the medium, no Cherenkov radiation is produced. Similarly, in the nonlinear optical process, the strong incident light field acts with the medium to polarize, and the nonlinear polarization intensity P_{NL} of the medium produces nonlinear polarization waves to become a harmonic sub-wave source to radiate out, and when the phase velocity of the nonlinear polarization waves exceeds that of the harmonics produced along the direction of the fundamental-frequency light, nonlinear Cherenkov radiation can be excited. Fig. 4 shows the automatic longitudinal matching of vector triangles generating nonlinear Cherenkov radiation, whose Cherenkov angle satisfies Eq. (4):

$$\cos\theta = \frac{v_2}{v_{np}} = \frac{v_2}{v_1} = \frac{2k_1}{k_2} = \frac{n_1}{n_2} \tag{4}$$

where v_1, v_{np} and v_2 are the phase velocities of the fundamental, the nonlinearly polarized wave and the second harmonic, respectively, and n_1 and n_2 are the refractive indices of the fundamental and the harmonics in the medium, respectively. From Eq. It can be seen that the generation of nonlinear Cherenkov radiation requires the refractive index of the fundamental wave to be smaller than the refractive index of the generated harmonics, i.e., the medium has to meet the normal dispersion condition in the light field band, which is also known as the dispersion limitation for the generation of nonlinear Cherenkov radiation. In terms of the inverse space, with the nonlinear Ramanas diffraction is similar in that the mismatch in the transverse direction of the fundamental wave propagation direction when viewed on the vector triangle is satisfied in the longitudinal direction by an automatic match, which is also a spatially partial phase match. Therefore, the nonlinear Cherenkov radiation belongs to the automatic longitudinal matching, and the outgoing angle of the harmonics is related only to the dispersion conditions of the medium and not to the lattice vectors in the crystal.

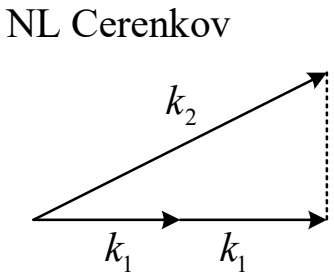

Figure 4: Diagram of nonlinear Cerenkov radiation

III. B. Basic form of the theoretical model

The nonlinear interaction of light with SOI waveguides can be described relatively accurately by the generalized nonlinear Schrödinger equation (GNLSE), which is applicable even for the case of ultrashort pulses generating an octave of the supercontinuum spectrum. Since the origin of the third-order nonlinear effects in SOI waveguides is very similar to that of quartz, the theoretical model of fiber-optic waveguide nonlinearity can be appropriately modified to satisfy the properties of silicon materials. For example, the unique properties encompassed by silicon as a semiconductor crystalline material include two-photon absorption (TPA), free-carrier absorption (FCA), free-carrier dispersion (FCD), anisotropy, and discrete third-order nonlinear features [119, 120].A more complete theoretical model of pulse transmission in SOI waveguides is shown in Equation (5):

$$\frac{\partial A_j}{\partial z} = \sum_{m=0}^{\infty} \frac{i^{m+1}\beta_{jm}}{m!} \frac{\partial^m A_j}{\partial t^m} + i\beta_j^f(\omega, N_e, N_h)A_j + i(1 + i\xi\frac{\partial}{\partial t})P_j^{NL} \tag{5}$$

In Equation (5), A_j denotes the amplitude of the pulse in the time domain and β_{jm} is the mth order dispersion parameter at the center frequency. The first term at the right end of the equation represents two physical meanings, the linear loss of the SOI waveguide (embodied in the imaginary part of parameter β_{jm}) and the linear dispersion of the waveguide mode (embodied in the real part of parameter section β_{jm}), the second term at the right end of the equation embodies the dispersion and loss due to free carriers, and the third term at the right end of the equation represents the third-order nonlinear effect.

Assuming that the produced free carriers are all photogenerated carriers, the following relation (6) is given for the produced free carrier concentration N. and the electron concentration (N_e) and hole concentration (N_b) are the same, i.e., $N_e = N_h = N_c$:

$$\beta_j^f(\omega, N_e, N_h) = \beta_j^f(\omega, N_c) \approx \frac{n_0(\omega)}{n_i(\omega)}\left[\frac{\omega}{c}n_f(\omega, N_c) + \frac{i}{2}\alpha_f(\omega, N_c)\right] \tag{6}$$

It is clear from the above equation that the real part of section β_j represents the free carrier dispersion and the imaginary part represents the free carrier absorption. The physical meanings of the other parameters are: n_0 represents the refractive index of silicon, n_i represents the mode refractive index. n_f represents the free carrier refractive index, which is related to the free carrier concentration N_c as in Eq. (7):

$$n_f = \sigma_n(\omega) N_c = \zeta \left(\frac{\omega_r}{\omega} \right)^2 N_c \tag{7}$$

where the parameter $\zeta = -1 - 35 \times 10^{-27} m^3$ when the wavelength is 1550 nm.

The free carrier absorption coefficient α_f has a similar mathematical expression to the free carrier refractive index (8):

$$\alpha_f = \sigma_a(\omega) N_c = 1 - 45 \times 10^{-21} \left(\frac{\omega_r}{\omega} \right)^2 N_c \tag{8}$$

The evolution of the average free carrier concentration can be determined by the following equation (9):

$$\frac{\partial N_c(z,t)}{\partial z} = \frac{\beta_{TPA}}{2h\nu_0} \frac{|A(z,t)|^4}{a_{eff}^2} - \frac{N_c(z,t)}{\tau_c} \tag{9}$$

where β_{TPA} is the two-photon absorption coefficient, a_{eff} is the effective area, and τ is the average lifetime of free carriers, which is affected by the combined effects of recombination, diffusion, and drift.

The third term at the right end of equation (5) embodies the third-order nonlinear effect, in which ξ is the frequency-dependent nonlinear parameter, and its expression is equation (10):

$$\xi \equiv \frac{1}{\omega_0} + \frac{1}{\chi_e(\omega_0)} \frac{d\chi_e}{d\omega} \Big|_{\omega_0} - \frac{1}{a_{eff}(\omega_0)} \frac{da_{eff}}{d\omega} \Big|_{\omega_0} \tag{10}$$

Eq. $\chi_e(\omega_0) \equiv \chi^e(-\omega_0; \omega_0, -\omega_0, \omega_0)$. In practice, parameter ξ is only important when the spectrum of the incident pulse broadens to a large extent during transmission through the SOI waveguide (e.g., supercontinuum generation). In many practical examples, the value of ξ is so small that its role can be neglected. The third term at the right end of Equation (5) also has a nonlinear polarization parameter P_j^{NL}, which has an expression in the time domain as in Equation (11):

$$P_j^{NL}(z,t) = A_k(z,t) \int_{-\infty}^{+\infty} R_{jklm}^3(t-\tau) A_l^*(z,\tau) A_m(z,\tau) d\tau \tag{11}$$

where $R_{jklm}{}^3$ is the third-order nonlinear response function, which can be written as equation (12):

$$\begin{aligned} R_{jklm}^3(t) = \gamma_e(\omega_0) \delta(\tau) \left[\frac{\rho}{3} (\delta_{jk}\delta_{lm} + \delta_{jl}\delta_{km} + \delta_{jm}\delta_{kl}) + (1-\rho)\delta_{jklm} \right] \\ + \gamma_R h_R(t) (\delta_{jl}\delta_{km} + \delta_{jm}\delta_{kl} - 2\delta_{jklm}) \end{aligned} \tag{12}$$

The nonlinear parameter $\gamma_e(\omega_0)$ can be defined as equation (13):

$$\gamma_e(\omega_0) \equiv \gamma_{1111}^e(-\omega_0; \omega_0, -\omega_0, \omega_0) \equiv \gamma_0(\omega_0) + i\beta_{TPA}(\omega_0)/(2a_{eff}) \tag{13}$$

$\gamma_0 = \omega_0 n_2 / (ca_{eff})$ is the nonlinear Kerr coefficient and the anisotropy parameter of silicon can be measured by $\rho = 1.27$. The contribution of Raman scattering to the third-order nonlinear response is mainly in parameter γ_R, and $h_R(t)$ is the Raman response function.

Equation (5) uses the direction along the crystal axis as the reference coordinate, and for commonly used wafers, the substrate is on the (100) plane, which means that the SOI waveguide is fabricated along the [0 1 0] and [0 0 1] directions. If the waveguide is not fabricated along the above directions, then the nonlinear response is rotated somewhat in other Cartesian coordinate systems. In general, SOI waveguides are designed and fabricated along the [0 1 1] direction for reasons such as ease of cutting.

Equation (5) provides a complete theoretical model for the study of nonlinear effects in SOI waveguides, and all kinds of nonlinear effect phenomena in SOI waveguides can be investigated with this model. Equation (5) can be further simplified to Eqs. (14)-(15) if the influence of the excited Raman scattering effect is not considered:

$$\frac{\partial A_x}{\partial z}=\sum_{m=0}^{\infty}\frac{i^{m+1}}{m!}\beta_{xm}\frac{\partial^m A_x}{\partial t^m}-\frac{\alpha_i}{2}A_x-\frac{\sigma}{2}(1+i\mu)N_c A_x +\frac{ik_0 n_2}{a_{eff}}(1+ir)\left(\frac{1+\rho}{2}|A_x|^2+\frac{\rho}{3}2|A_y|^2\right)A_x \tag{14}$$

$$\frac{\partial A_y}{\partial z}=\sum_{m=0}^{\infty}\frac{i^{m+1}}{m!}\beta_{ym}\frac{\partial^m A_y}{\partial t^m}-\frac{\alpha_l}{2}A_y-\frac{\sigma}{2}(1+i\mu)N_c A_y +\frac{ik_0 n_2}{a_{eff}}(1+ir)\frac{\rho}{3}(|A_y|^2+2|A_x|^2)A_y \tag{15}$$

In the set of equations (14) and (15), $j=x$ and $j=y$ denote the TE mode component and TM mode component, respectively, and in the third-order nonlinear response terms represented by the equations, the first term in curly brackets denotes the self-phase modulation (SPM) effect, and the second term denotes the cross-phase modulation effect (XPM) and the crossed two-photon absorption effect (XTPA).

IV. Numerical simulation of nonlinear optical effects in different solid state physics

Supported by the numerical analysis technique (finite element modeling) and the theoretical modeling framework of nonlinear optical effects presented above, this chapter sequentially carries out the nonlinear optical analysis and application studies of graphene, graphyne, and materials.

IV. A. Efficient four-wave mixing generation in graphene

Figure 5 depicts the trend of the amplitudes of the probe field and the four-wave mixing signal field with penetration depth z in the graphene system with the added magnetic field. The amplitude of the probe field decreases monotonically with the increase of z at the beginning, while the amplitude of the four-wave mixing field increases monotonically with the increase of z at the beginning, and finally both of them reach the saturation value and then no longer change with the increase of z. The reason is due to the quantum destructive interference due to the competition between the phase-length and phase-canceling interferences induced by two different excitation channels (coupled excitation channel and feedback-coupled excitation channel). When the generated four-wave mixing signal is strong enough after propagating a certain distance, the feedback-coupled excitation channel differs by π from the coupled excitation channel in phase $|1\rangle\rightarrow|2\rangle$, which provides a destructive interference pathway that suppresses the amplitude of the energy band $|4\rangle$ that generates the four-wave mixing.

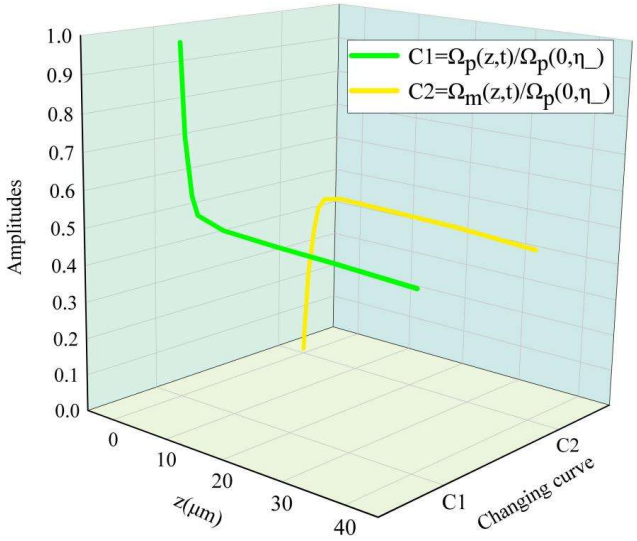

Figure 5: Detect the changes in the intensity of the field and the signal field

The other parameters are: $\gamma_3=0.5\times10^{13}s^{-1}$, $|\Omega_c|=|\Omega_d|=18\gamma_3$, $\gamma_2=\gamma_3=\gamma_4$, $\Delta_p=\Delta_c=\Delta_d=0$, $K_p=K_m=\gamma_3\mu m^{-1}$.

Figure 6 shows the absorption coefficient ratios as a function of the pump field Rabi energy $|\Omega_c|$. The trend of the two absorption coefficient ratios $\alpha_+ / \alpha_- = \mathrm{Im}[K_-(0)] / \mathrm{Im}[K_+(0)]$ with respect to the probe field Rabi energy $|\Omega_c|$ is simulated numerically given several different values of the pump field $|\Omega_d|$. As can be seen from the figure, one of the modes α_+ decays very fast $(\alpha_+ \square \alpha_-)$ compared to the other α_-, so that this fast variable K_+ can be neglected after propagating a small distance. Since the K_- modes of the probe field and the four-wave mixing field are of the same form, the matching group velocity of the two pulses during propagation is $V_g = V_-$. When this fast variable K_+ is neglected, the probe field and the mixing field become Eqs. (16)-(17):

$$\Omega_p(z,t) = \Omega_p(0,\eta_+)U_+(0)e^{K,(0)} - \Omega_p(0,\eta_-)U_-(0)e^{K,(0)} \tag{16}$$

$$\Omega_m(z,t) = S(0)(\Omega_p(0,\eta_+)e^{K,(0)} - \Omega_p(0,\eta_-)U_-(0)e^{K,(0)}) \tag{17}$$

where is the $\alpha = \mathrm{Im}[K_-(0)]$ absorption coefficient, and $\beta = R\mathrm{e}[K_-(0)]$ and $V_g = 1/R\mathrm{e}[K_-^{(1)}]$ denote the phase shift and group velocity per unit of length, respectively.

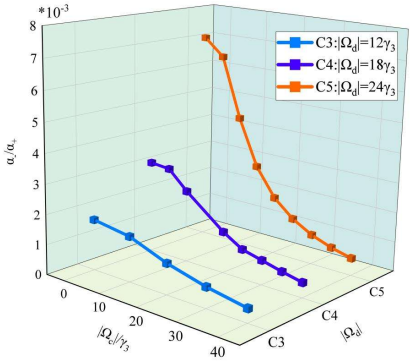

Figure 6: The absorption coefficient ratio is a function of $|\Omega_c|$

Based on the above results, the variation of the relative group velocity with the pump field Rabi energy $|\Omega_c|$ is depicted in Fig. 7, which realizes the ultra-slow transmission of the probe and mixing fields, where the group velocity is of the order of 10-3 c. The emergence of the ultra-slow transmission is mainly due to the multiphoton quantum-destructive interference generated by the driving of the two pump fields that changes the dispersion property of graphene, resulting in the ultra-slow propagation of the group velocity. The other pump field Rabi energy $|\Omega_d|$ is taken as $|\Omega_d|$=$12\gamma_3$, $18\gamma_3$, and $24\gamma_3$, and the other parameters are γ_3=$0.5\times10^{13}s^{-1}$, $\gamma_2 = \gamma_3 = \gamma_4$, $\Delta_p = \Delta_c = \Delta_d = 0$, and $K_p = K_m = \gamma_3\mu m^{-1}$, respectively.

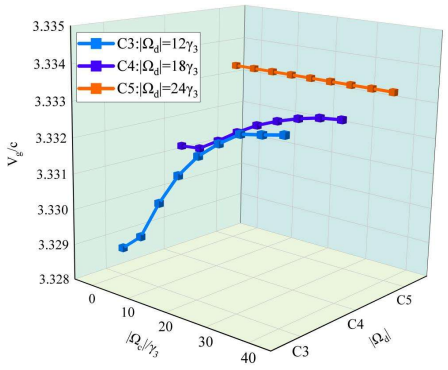

Figure 7: A function of the relative group velocity with respect to $|\Omega_c|$

IV. B. Passive mode-locked fiber laser output based on graphyne

During the study of the output characteristics of a mode-locked fiber laser based on graphyne, the PC is appropriately adjusted to achieve self-started mode-locking. In the experiment, a continuous wave signal can be observed by gradually increasing the pump power when the intracavity loss is reduced to a low level. Subsequently, by continuing to increase the pump power to about 140 mW, a stable soliton mode-locked spectrum appeared, and the output characteristics of the laser pulse are shown in Fig. 8. Soliton mode-locking was observed for the erbium-doped fiber laser at the repetition frequency (22.5 MHz) of the resonant cavity. Figure 8(a) shows a typical pulse train of the laser, and the oscilloscope shows a uniform pulse spacing during the experiment, which proves that there is no mode-locking in the laser during the experiment. And the time interval between the two pulses is 44.9 ns.The spectral characteristics of the output pulse are given in Fig. 8(b), which shows a center wavelength of 1558.8 nm and a 3 dB bandwidth of 8.7 nm. Soliton mode-locking was achieved using a graphyne saturable absorber. Fig. 8(c) shows the autocorrelation trajectory measured using the autocorrelator by hyperbolic secant fitting (sech²) with a pulse width of 324.7 fs after function fitting. In addition, the RF spectrum of the erbium-doped fiber passive mode-locked laser was measured in the experiment shown in Fig. 8(d), and the measured signal-to-noise ratio of the mode-locked pulses was 80 dB without any harmonics, which proved that the laser could maintain mode-locking for a long time.

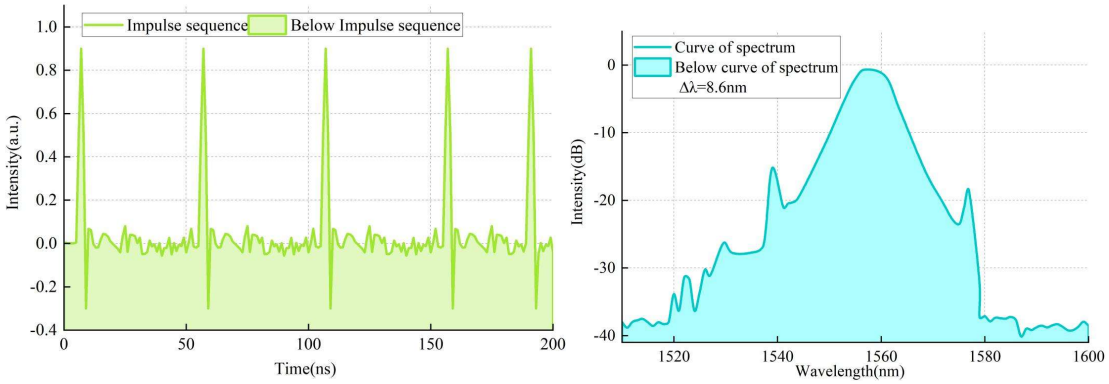

(a) A typical pulse sequence (b) Laser output spectrum

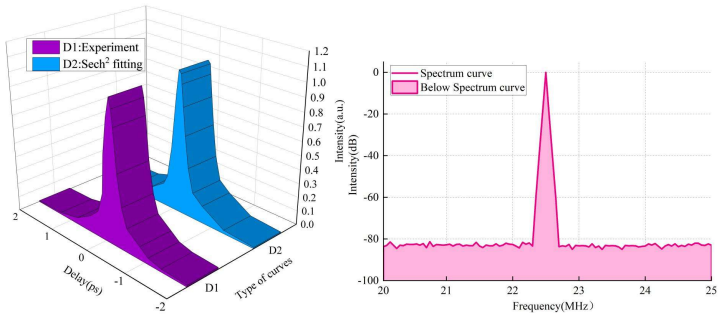

(c) Autocorrelation curve (d) Output spectrum

Figure 8: The output performance of an erbium-doped fiber laser

In the experiment, the output power and pulse energy of the passive mode-locked fiber laser were measured in Fig. 9. When the pump power changes, the output power and pulse energy of the laser also change. When the pump power increased, the output power and pulse energy showed an increasing trend, and its maximum average output power and maximum pulse energy were 2.3 1 mW and 0.11 nJ, respectively.

In addition, the output power stability was measured during the experiment. The output power was continuously monitored for 10 hours using a power meter, and the specific measurement data are shown in Fig. 10. It can be observed in the figure that the output power was basically maintained at 2.31 mW, which proves the excellent stability of the laser in the experiment.

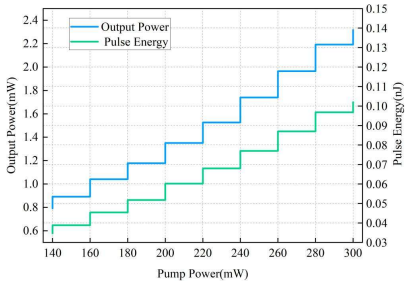

Figure 9: The output power and pulse energy of laser

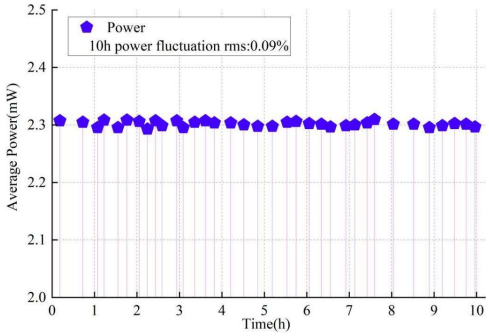

Figure 10: Power stability of the laser

IV. C. Analysis of ferroelectric properties of materials

The monolayers of group V elements are extraordinarily flexible due to their symmetry and elasticity, and the distorted structures are characterized by in-plane spontaneous polarization. Among them, the optimized structures of the FE and FE' phases undergo a structural distortion compared to the PE phase structure. This distortion can be seen as a vertical shift of the red atoms on the nearby yellow atoms. In this case, the structural distortion occurs only along the out-of-plane direction, while it remains constant along the in-plane. The calculated contributions of electrons and ions to the total polarization in different directions are shown in Fig. 11.According to Fig. 11(a), the contribution of ions to the x-component of the electrode polarization is zero due to the fact that no structural distortion occurs along the x-direction. In addition, since the system has mirror symmetry with respect to x, i.e., $(x, y) \rightarrow (-x, y)$ and the charge distribution is symmetric along the x direction, the electronic part contribution is also zero for the x component of the polarization. For along the y-direction, the ionic contribution can also be observed similarly to the x-direction, as in Fig. 11(b), however, at this point the electronic part is no longer zero but exhibits ferroelectric switching properties along the phase transition path, which can be attributed to the breaking of the inversion symmetry leading to the redistribution of the charge. As for the z-component, as in Fig. 11(c), since the structural distortion occurs along the z-direction, both electrons and ions contribute to the electrode polarization, but with opposite magnitude and direction, and thus the total electrode polarization remains zero throughout the phase transition. These results indicate that although the ferroelectricity of the monolayer of group V elements is caused by structural distortion, the total polarization is caused by the electronic part and only the y component is not zero.

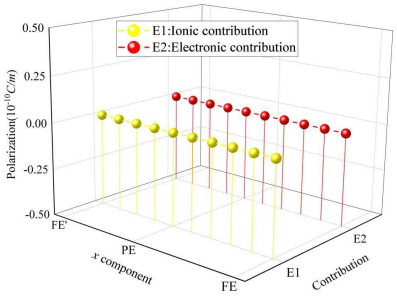

(a) x component

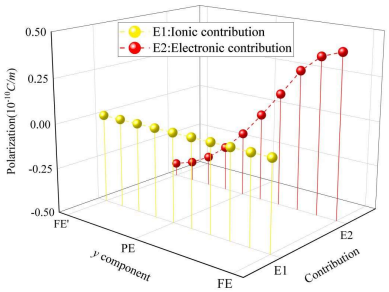

(b) y component

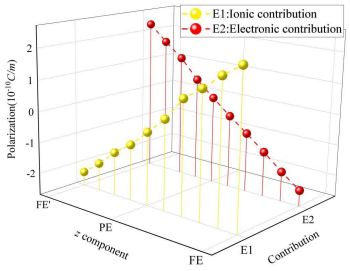

(c) z component

Figure 11: The variation of ferroelectric polarization of the three components

V. Conclusion

In this paper, a solid physics-based finite element analysis model is constructed through the use of finite element numerical analysis techniques that organically combine elasticity theory, mathematics and computer software. Combined with the theoretical modeling framework of various nonlinear optical effects established, the proposed analytical method for nonlinear optical effects on solid physical materials is proposed.

The proposed analytical method is applied to the analysis of nonlinear optical effects in different solid state physics, and the four-wave mixing field expression for the ultra-slow propagation of graphene material in the steady state case is obtained: $\Omega_m(z,t) = S(0)(\Omega_p(0,\eta_+)e^{K,(0)} - \Omega_p(0,\eta_-)U_-(0)e^{K,(0)})$. The stability of a laser based on the nonlinear optical properties of graphene is also verified (the output power is stabilized at 2.31 mW within 10 h). The polarization-dependent bulk photovoltaic effect in ferroelectric materials is also established by analyzing the linear relationship of electrode polarization in monolayers of group V elements.

References

[1] Li, C. (2017). Nonlinear optics. Principles and Applications.

[2] Zhang, Y., Xu, D. D., Tanriover, I., Zhou, W., Li, Y., López-Arteaga, R., ... & Mirkin, C. A. (2025). Nonlinear optical colloidal metacrystals. Nature Photonics, 19(1), 20-27.

[3] Aslam, H. Z., Doane, J. T., Yeung, M. T., & Akopov, G. (2023). Advances in solid-state nonlinear optical materials: from fundamentals to applications. ACS Applied Optical Materials, 1(12), 1898-1921.

[4] Reshef, O., De Leon, I., Alam, M. Z., & Boyd, R. W. (2019). Nonlinear optical effects in epsilon-near-zero media. Nature Reviews Materials, 4(8), 535-551.

[5] Zhang, Y. X., & Wang, Y. H. (2017). Nonlinear optical properties of metal nanoparticles: a review. RSC advances, 7(71), 45129-45144.

[6] Guo, B., Xiao, Q. L., Wang, S. H., & Zhang, H. (2019). 2D layered materials: synthesis, nonlinear optical properties, and device applications. Laser & Photonics Reviews, 13(12), 1800327.

[7] Dong, X., Huang, L., & Zou, G. (2024). Rational design and controlled synthesis of high-performance inorganic short-wave UV nonlinear optical materials. Accounts of Chemical Research, 58(1), 150-162.

[8] Guo, S. P., Chi, Y., & Guo, G. C. (2017). Recent achievements on middle and far-infrared second-order nonlinear optical materials. Coordination Chemistry Reviews, 335, 44-57.

[9] Kang, L., Liang, F., Jiang, X., Lin, Z., & Chen, C. (2019). First-principles design and simulations promote the development of nonlinear optical crystals. Accounts of Chemical Research, 53(1), 209-217.

[10] Wu, J., Li, Z. A., Luo, J., & Jen, A. K. Y. (2020). High-performance organic second-and third-order nonlinear optical materials for ultrafast information processing. Journal of Materials Chemistry C, 8(43), 15009-15026.

[11] Bano, R., Asghar, M., Ayub, K., Mahmood, T., Iqbal, J., Tabassum, S., ... & Gilani, M. A. (2021). A theoretical perspective on strategies for modeling high performance nonlinear optical materials. Frontiers in Materials, 8, 783239.

[12] Morimoto, T., & Nagaosa, N. (2016). Topological nature of nonlinear optical effects in solids. Science advances, 2(5), e1501524.

[13] Biswas, B., Ahmed, K., Paul, B. K., Khalek, M. A., & Uddin, M. S. (2019). Numerical evaluation of the performance of different materials in nonlinear optical applications. Results in Physics, 13, 102184.

[14] Sun, Y., Dong, M., Yu, M., Lu, L., Liang, S., Xia, J., & Zhu, L. (2021). Modeling and simulation of all-optical diffractive neural network based on nonlinear optical materials. Optics Letters, 47(1), 126-129.

[15] Hou, E., Wang, F., Salama, S. A., & Khater, M. M. (2022). On analytical and numerical simulations for the ultra-short pulses mathematical model in optical fibers. Fractals, 30(05), 2240141.